Optical detection of rate-determining ion-modulated conformational changes of the ether-à-go-go K⁺ channel voltage sensor

John P. A. Bannister*, Baron Chanda*†, Francisco Bezanilla*†, and Diane M. Papazian*‡

Departments of *Physiology and †Anesthesiology, Geffen School of Medicine, University of California, Los Angeles, CA 90095-1751

In voltage-dependent ether-à-go-go (eag) K⁺ channels, the process of activation is modulated by Mg²⁺ and other divalent cations, which bind to a site in the voltage sensor and slow channel opening. Previous analysis of eag ionic and gating currents indicated that Mg²⁺ has a much larger effect on ionic than gating current kinetics. From this, we hypothesized that ion binding modulates voltage sensor conformational changes that are poorly represented in gating current recordings. We have now tested this proposal by using a combined electrophysiological and optical approach. We find that a fluorescent probe attached near S4 in the voltage sensor reports on two phases of the activation process. One component of the optical signal corresponds to the main charge-moving conformational changes of the voltage sensor. This is the phase of activation that is well represented in gating current recordings. Another component of the optical signal reflects voltage sensor conformational changes that occur at more hyperpolarized potentials. These transitions, which are rate-determining for activation and highly modulated by Mg²⁺, have not been detected in gating current recordings. Our results demonstrate that the eag voltage sensor undergoes conformational changes that have gone undetected in electrical measurements. These transitions account for the time course of eag activation in the presence and absence of extracellular Mg²⁺.

activation | voltage-gated

Drosophila ether-à-go-go (eag) is the original member of a subfamily of voltage-dependent K⁺ channels that includes eag, eag-related gene (erg), and eag-like (elk) channels (1, 2). In mammals, these channels are expressed in the brain and heart, where they play key roles in controlling excitability (2–4). For example, human erg (HERG) channels contribute significantly to the repolarization of the cardiac action potential (3). Disruption of HERG activity results in long QT syndrome, a predisposition to cardiac arrhythmia and sudden death (3, 5, 6).

Eag channels comprise four subunits surrounding a central pore for K⁺ permeation (7). Each subunit has six transmembrane segments. The last two transmembrane segments (S5 and S6) and the intervening P loop form the ion selective pore, whereas S1–S4 form the voltage sensor (8, 9). Voltage control of channel activity is primarily due to the S4 segment, which contains multiple positively charged residues (10). In response to changes in transmembrane voltage, charged residues in S4 initiate conformational changes that control whether the pore is open or closed (11, 12). S4 conformational changes can be measured electrically as gating currents (13).

Channels in the eag subfamily are subject to a novel form of regulation by extracellular divalent cations (14–16). In eag channels, the process of voltage-dependent activation is modulated directly by binding of divalent cations to a site in the voltage sensor (16, 17). Extracellular divalent ions, including Mg²⁺, Mn²⁺, and Ni²⁺, slow activation kinetics (14, 18). The half-maximal effective concentration of Mg²⁺ closely matches its normal physiological concentration (17, 18). We have shown that bound ions interact with eag-specific acidic residues in trans-

membrane segments S2 and S3 (Fig. 1*A*) and have presented evidence that ion binding directly modulates S4 conformational changes (17, 19). Interestingly, ion binding slows the kinetics of both ionic and gating currents, but the magnitude of the effect on ionic currents is much greater than on gating currents (16). From these results, we hypothesized that ion binding may significantly modulate voltage sensor conformational changes that are poorly represented in gating current measurements, presumably because the transitions are too slow or move too little gating charge to be readily detected. We have now tested this hypothesis by using an optical method. We find that ion binding modulates rate-limiting conformational changes of the voltage sensor that occur at hyperpolarized potentials and are not detected electrically in gating current measurements. These optically detected transitions account for the different kinetics of eag activation in the presence and absence of extracellular Mg²⁺.

Materials and Methods

Mutations were introduced by using the QuickChange (Stratagene) technique and confirmed by DNA sequencing. RNA was prepared and injected into *Xenopus* oocytes by using standard methods (16). Ionic currents were recorded at room temperature (20–22°C) 1–2 days after injection by using a two-electrode voltage clamp or a cut-open oocyte voltage clamp equipped with epifluorescence (20–23).

For the two-electrode voltage clamp, oocytes were bathed in 89 mM KCl/29 mM NaCl/1.8 mM CaCl₂/10 mM Hepes, pH 7.2, with or without 10 mM Mg²⁺, as noted. Electrodes contained 3 M KCl and had resistances of 0.3–0.8 MΩ. Ionic currents were evoked by stepping from the holding potential of −90 mV to the indicated prepulse potentials for 100 ms before depolarization to the test potential for 150 ms. Linear capacitative and leak currents were subtracted by a P/−4 protocol (24). Data were filtered at 2 KHz and sampled at 10 KHz.

For optical analysis, oocytes were labeled for 45 min on ice with 50 µM tetramethylrhodamine maleimide (TMRM) in the 89-mM KCl solution described above and washed with ND-96 (23, 25). Ionic currents, gating currents, and fluorescent intensity were recorded by using the CA-1B cut-open voltage clamp (Dagan Instruments, Minneapolis). Saponin (0.3%) was briefly applied in the lower chamber to provide electrical access to the oocyte interior. During recordings, the lower chamber contained 120 mM K-Mes, 2 mM EGTA, and 20 mM Hepes, pH 7.2. The upper and guard chambers contained 10 mM K-Mes, 79 mM N-methylglucamine-Mes, 1.8 mM CaCl₂, and 10 mM Hepes, pH 7.2, with or without 10 mM Mg²⁺. For gating current recordings, tetraethylammonium-Mes was substituted for K-Mes. Recordings were made by stepping from the holding potential of −90
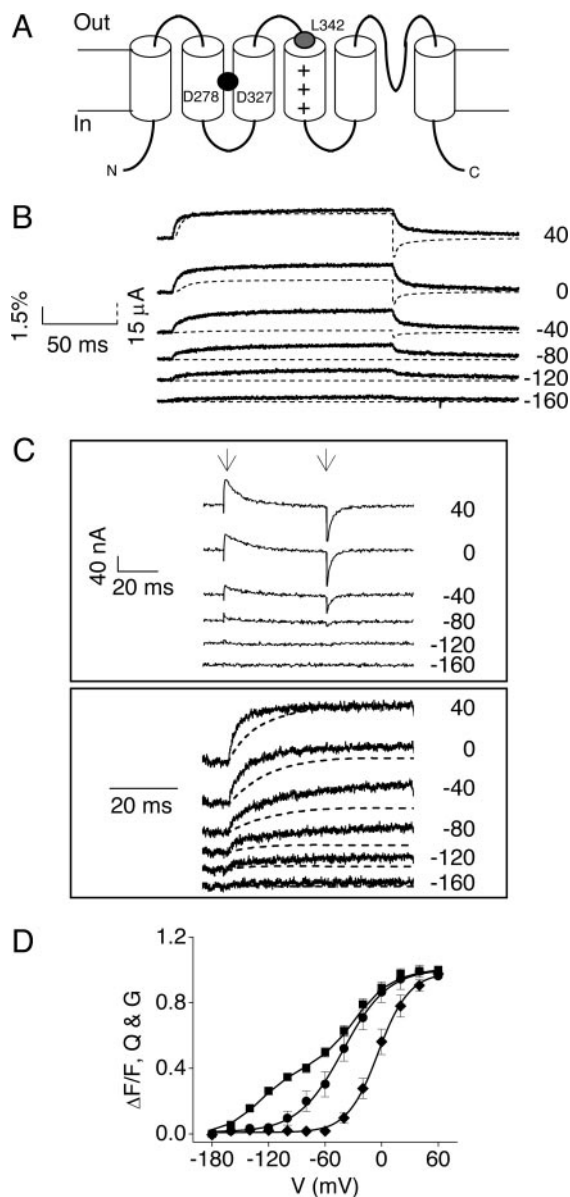
Fig. 1. Voltage-dependent $\Delta F/F$ signal from TMRM-L342C channels. (*A*) Schematic representation of eag, showing the approximate locations of the Mg^{2+}-binding site (black circle) and the L342C mutation (gray circle) (17). Positively charged residues in S4 are indicated by "+." (*B*) Ionic current (dashed) and $\Delta F/F$ traces (solid) were recorded simultaneously in the absence of extracellular Mg^{2+}. After a 100-ms prepulse to −180 mV, the membrane was stepped to the indicated voltages for 150 ms. Representative data are shown. (*C*) (*Upper*) Gating current traces were recorded in the absence of Mg^{2+} by stepping from −180 mV to the indicated voltages. The arrows indicate the region integrated to obtain the time course of gating charge movement, shown at bottom. (*Lower*) Gating currents and $\Delta F/F$ were recorded simultaneously. The time course of gating charge movement (dashed) was overlaid with the $\Delta F/F$ trace (solid). The gating current and $\Delta F/F$ traces were scaled to the same amplitude at +40 mV, and this amplitude was used to normalize data obtained at other voltages. Representative data are shown. (*D*) Normalized steady-state $G–V$ (diamonds), $Q–V$ (circles), and $\Delta F/F–V$ (squares) curves were obtained in the absence of Mg^{2+}. Solid lines represent fits of single ($G–V$ and $Q–V$) or double ($\Delta F/F–V$) Boltzman functions. Fitted values of $V_{1/2}$ were −33 ± 3 mV and −3 ± 1 mV and apparent valences were 0.9 ± 0.1 and 1.5 ± 0.1 for the $Q–V$ and $G–V$ curves, respectively. Double Boltzmann fits of the $\Delta F/F–V$ data yielded $V_{1/2}$ values of −130 ± 4 mV and −30 ± 3 mV for the hyperpolarized and depolarized components, respectively, and apparent valences of 0.8 ± 0.1 for both components. Data are presented as mean ± SEM, $n = 4–9$. If error bars are not visible, they are smaller than the size of the symbol.

mV to −180 mV for 100 ms, before stepping to the test potential for 150 ms. For gating currents, the test pulse was decreased to 50 ms. Electrical and optical signals were acquired at 5 μs per point and digitally filtered at cutoff frequencies of 20 and 10 KHz for optical and electrical signals, respectively (26). Traces were averages of three to six sweeps. Ionic current records were leak- and capacity-subtracted by using a P/−4 protocol with a subtraction potential of −180 mV (24). Gating current traces were leak-subtracted by using a P/+4 protocol with a subtraction potential of +60 mV. In addition, capacitive currents were compensated online. Fluorescence traces were corrected for background photobleaching. Values of ΔF were divided by the total fluorescence (F) at time 0 for each sweep to obtain $\Delta F/F$, thus correcting for changes in F intensity due to bleaching during the course of the experiment. As noted, $\Delta F/F$ values were normalized to the maximum $\Delta F/F$ values obtained at +60 mV. Corrected data were digitally filtered at 1 KHz.

The steady-state $\Delta F/F$ data were fitted with the sum of two Boltzmann functions by using an equation of the form:

$$y = (A_H/[1 + \exp[z_H(V_{1/2H} − V)/25.35]])$$
$$+ (A_D/[1 + \exp[z_D(V_{1/2D} − V)/25.35]]),$$

where A_H, $V_{1/2H}$, and z_H correspond to the amplitude, midpoint voltage, and apparent valence of the hyperpolarized component, and A_D, $V_{1/2D}$, and z_D, the same parameters for the depolarized component. The number 25.35 corresponds to the value of RT/F, where R is the universal gas constant, T the temperature, and F the Faraday constant, at room temperature.

The $G–V$ and $Q–V$ data were fitted with a single Boltzmann function of the form:

$$y = ([A_i − A_f]/[1 + \exp[z(V_{1/2} − V)/25.35]]) + A_f,$$

where A_i and A_f correspond to the initial and final amplitudes, respectively, $V_{1/2}$ is the half activation voltage, and z is the apparent valence.

$\Delta F/F$ kinetics were fitted with a double-exponential function of the form:

$$y = A_{fast}[1 − \exp(−t/\tau_{fast})] + A_{slow}[1 − \exp(−t/\tau_{slow})],$$

where A_{fast} and A_{slow} correspond to the amplitudes and τ_{fast} and τ_{slow} to the time constants of the fast and slow components, respectively, and t is time. To characterize the development of $\Delta F/F$ kinetics as a function of voltage, coefficients of the fast and slow components were calculated as follows. The values of A_{fast} and A_{slow} at each test voltage were divided by the maximal ΔF value for that cell obtained by pulsing from −180 to +60 mV. These coefficients were summed to give $A_\tau/\Delta F_{+60\,mV}$, which was plotted versus test voltage.

Ionic current kinetics were fitted with a single exponential function of the form:

$$y = A_{ionic}[1 − \exp(−t/\tau_{ionic})] + B,$$

where A_{ionic} is the amplitude, τ_{ionic} is the time constant, t is time, and B corresponds to the amplitude at the start of the fit.

Results

TMRM-L342C Channels Exhibit Robust Voltage-Dependent Changes in Fluorescent Intensity. Voltage sensor conformational changes have traditionally been characterized by gating current recordings, which provide an electrical measurement of the movement of charged amino acids in the voltage sensor (13). More recently, voltage sensor conformational changes have been inferred from optical recordings of the fluorescent intensity of fluorophores attached in proximity to the voltage sensor (23, 25, 27–29). In

Shaker, bovine eag, and human eag-related gene channels, such measurements have revealed voltage-dependent changes in fluorescent intensity that correlate fairly well with the steady-state and/or kinetic properties of ionic or gating currents (23, 25, 27–29). In most cases, these optical signals reflect changes in quenching of the fluorescent probe as a result of voltage sensor conformational changes (23).

To facilitate optical analysis of eag gating, channel expression was boosted 2- to 3-fold by engineering a consensus Kozak sequence (GCCACC) at the 5′ end of the ORF (data not shown) (30). Before site-directed labeling of the eag protein at an engineered cysteine, we incubated wild-type eag with TMRM. Upon subsequent analysis, no voltage-dependent changes in fluorescent intensity were detected (see Fig. 7, which is published as supporting information on the PNAS web site).

To attach a fluorophore near the voltage sensor in eag, we substituted L342, located at the N-terminal end of S4, with a cysteine residue (Fig. 1A). The L342C construct was expressed in *Xenopus* oocytes, labeled with TMRM and analyzed by using a two-electrode voltage clamp or a cut-open oocyte voltage clamp equipped with epifluorescence. The kinetics of activation and the voltage dependence and slope of the conductance-voltage (G-V) curve were very similar in wild-type and L342C channels. These parameters were not significantly altered by labeling L342C channels with TMRM (see Fig. 8, which is published as supporting information on the PNAS web site).

Simultaneous measurements of ionic currents and fluorescent intensity using the cut-open oocyte set up revealed that TMRM-labeled L342C channels exhibit a robust voltage-dependent change in fluorescent intensity ($\Delta F/F$) (Fig. 1B). From a holding potential of −90 mV, the membrane was stepped to −180 mV for 100 ms before a 150-ms depolarization to voltages ranging from −160 to +60 mV in 20-mV increments. A voltage-dependent $\Delta F/F$ signal was detected at −160 mV and at more positive voltages. Ionic current was detected at −40 mV and at more positive voltages. Thus, $\Delta F/F$ was detected at voltages that did not lead to noticeable pore opening. The time course of the $\Delta F/F$ signal preceded activation of the ionic current.

The identification of a $\Delta F/F$ signal that was detectable at voltages more negative than channel opening and that preceded the time course of the ionic current is consistent with the idea that $\Delta F/F$ reports conformational changes of the eag voltage sensor. To compare the $\Delta F/F$ signal to gating charge movement, eag ionic current was blocked by addition of tetramethylammonium ion to the intracellular and extracellular solutions, and simultaneous measurements of fluorescent intensity and gating currents were made (Fig. 1C). To compare the time courses of gating charge movement and the $\Delta F/F$ signal, gating current records were integrated as a function of time to give the extent of charge movement, and plotted together with $\Delta F/F$ data. At potentials where gating currents were detected, much of the $\Delta F/F$ signal preceded gating charge movement.

In addition to the $\Delta F/F$ signal obtained in the voltage range where gating currents were detected, a component of the voltage-dependent $\Delta F/F$ signal was detected at more hyperpolarized potentials (Fig. 1C). The steady-state properties of the voltage-dependent $\Delta F/F$ signal were compared with the G–V and gating charge-voltage (Q–V) curves (Fig. 1D). As reported (16), the Q–V curve is displaced to more negative voltages than the G–V curve, an indication that the channel transits through several closed conformations before opening. The $\Delta F/F$–V curve was also displaced to more negative voltages than the G–V curve and clearly contained two components. One component appeared to overlap the Q–V curve, whereas an additional component of the $\Delta F/F$–V curve was found at more hyperpolarized potentials where gating charge movement was not detected.

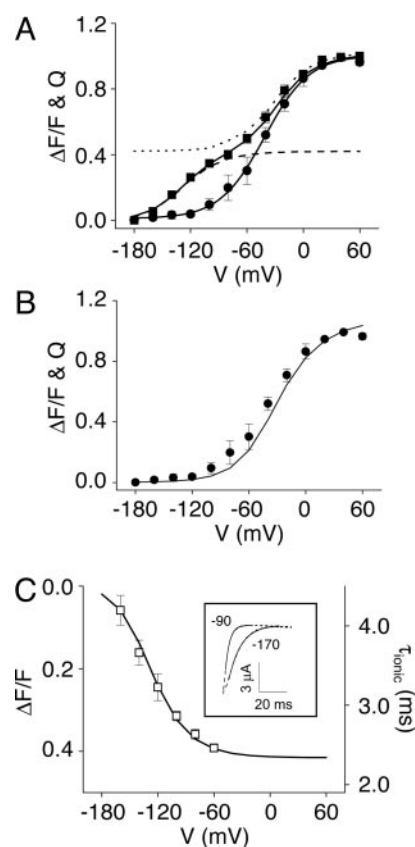The $\Delta F/F$–V data were well fitted by the sum of two Boltz-

Fig. 2. Steady-state components of $\Delta F/F$. (A) The fitted depolarized (dotted) and hyperpolarized (dashed) steady-state components of $\Delta F/F$ are shown, with the normalized $\Delta F/F$–V (squares) and Q–V (circles) curves from Fig. 1D for comparison. (B) The normalized Q–V data points (circles) are compared with the fitted depolarized steady-state component of $\Delta F/F$ (solid line), which has been scaled to an amplitude of 1.0. Q–V data are presented as mean ± SEM, n = 4. (C) (*Inset*) Representative ionic currents (dashed) were recorded at +60 mV after prepulses to the indicated potentials. Values for τ_{ionic} were determined from single exponential fits (solid lines). The main graph plots τ_{ionic} (open squares) as a function of prepulse potential. For comparison, the fitted hyperpolarized steady-state component of $\Delta F/F$ (solid line) is also shown. Values of τ_{ionic} are presented as mean ± SEM, n = 4. If error bars are not visible, they are smaller than the size of the symbol.

mann components (Fig. 1D). The individual fitted components, which will be referred to as the depolarized and hyperpolarized components based on their voltage dependencies, are shown in Fig. 2A. When the Q–V curve and the fitted depolarized component of the $\Delta F/F$–V curve were scaled to the same amplitude, it was apparent that the voltage dependencies of the detectable gating charge movement and the depolarized component of $\Delta F/F$ are virtually identical (Fig. 2B). This suggests that the depolarized component of the $\Delta F/F$ signal reports the main charge-moving conformational changes of the eag voltage sensor. In contrast, as mentioned above, the hyperpolarized component of $\Delta F/F$ occurred over a voltage range where no gating charge movement could be detected (Fig. 1D).

$\Delta F/F$ Signal Reports Voltage Sensor Transitions That Have Not Been Detected in Gating Current Measurements. The hyperpolarized component of $\Delta F/F$ may reflect rate-determining ion-modulated conformational changes of the voltage sensor that occur too slowly or move too little gating charge to be detected in gating current recordings. If so, these transitions could account for the quantitative discrepancy between the effects of divalent ions on the kinetics of the ionic and gating currents (16).

To test the hypothesis that the hyperpolarized component of $\Delta F/F$ reflects transitions in the activation pathway of eag, we compared its voltage dependence with the range of hyperpolarized potentials that alter activation kinetics (the Cole–Moore effect) (31). This approach was previously used to demonstrate that gating currents are associated with the opening of Na$^+$ channels (32). From a holding potential of -90 mV, 100-ms prepulses to potentials ranging from -170 to -60 mV were applied before a 50-ms test pulse to $+60$ mV. Ionic current kinetics at $+60$ mV were quantified by fitting a single exponential component to the traces (Fig. 2C Inset). Because the initial phase of eag current activation is highly sigmoidal, this phase was not included in the fit (14, 16). The fitted time constants (τ_{ionic}) were plotted as a function of prepulse potential (Fig. 2C). As previously reported, prepulse hyperpolarization slowed the kinetics of activation in eag, indicating that rate-determining transitions for activation are accessed at these potentials (16). To compare the voltage dependence of the Cole–Moore effect with that of the fitted hyperpolarized component of $\Delta F/F$, the hyperpolarized $\Delta F/F$ component was scaled, inverted, and plotted on the same axes (Fig. 2C). The voltage dependencies of the Cole–Moore effect and the hyperpolarized component of $\Delta F/F$ overlapped closely. This result supports the conclusion that the hyperpolarized component of $\Delta F/F$ reports voltage sensor conformational changes that are part of the eag activation pathway despite the fact that gating currents have not been detected in this voltage range. It also suggests that the hyperpolarized component of the $\Delta F/F$ signal is related to the rate-determining transition(s) accessed during prepulse hyperpolarization.

The excellent match between the hyperpolarized component of $\Delta F/F$ and the Cole–Moore effect and the depolarized component and the main charge-moving transitions of the voltage sensor suggests that the components of the $\Delta F/F$ signal reliably report the transitions responsible for activation of eag channels.

Kinetics of $\Delta F/F$ Signal Are Modulated by Mg^{2+}. To determine whether the conformational changes reported by the $\Delta F/F$ signal are sensitive to divalent ions, the kinetics of $\Delta F/F$ were characterized in the absence and presence of 10 mM Mg^{2+}. The kinetics of the $\Delta F/F$ signal were well fitted by two exponential components, providing values for two time constants, τ_{fast} and τ_{slow} (Fig. 3A). The values of τ_{fast} and τ_{slow} exhibited bell-shaped dependencies on voltage, with τ_{slow} showing a more hyperpolarized voltage dependence than τ_{fast} (Fig. 3B). This result suggests that τ_{slow} and τ_{fast} reflect the kinetics of the hyperpolarized and depolarized steady-state components of $\Delta F/F$, respectively. To test this hypothesis, we characterized the development of $\Delta F/F$ kinetics as a function of voltage. The absolute values of A_{fast} and A_{slow} at each test voltage were divided by the maximal ΔF value obtained by pulsing from -180 to $+60$ mV. These values were summed to yield $A_\tau/\Delta F_{+60\ mV}$ and plotted versus test voltage. As shown in Fig. 3C, there was no significant difference between the steady-state $\Delta F/F$–V and the kinetic $A_\tau/\Delta F_{+60\ mV}$–$V$ curves. We conclude that the fast and slow kinetic components of the $\Delta F/F$ signal correspond to the depolarized and hyperpolarized steady-state components, respectively.

Extracellular Mg^{2+} slowed activation kinetics in TMRM-labeled L342C channels (Fig. 4A Inset), although the magnitude of the effect was somewhat reduced compared with wild-type channels (see Fig. 8). Similar to activation of the ionic current, the time course of the $\Delta F/F$ signal was slowed by Mg^{2+} (Fig. 4A). Mg^{2+} had a differential effect on the two kinetic components of the $\Delta F/F$ signal (Fig. 4B). Mg^{2+} shifted the voltage dependence of τ_{slow} in the depolarized direction with little or no change in the values of τ_{slow}. The magnitude of the shift was ≈ 60 mV, which was estimated by comparing the voltages at which the maximum value of τ_{slow} was obtained in the absence and presence of Mg^{2+}
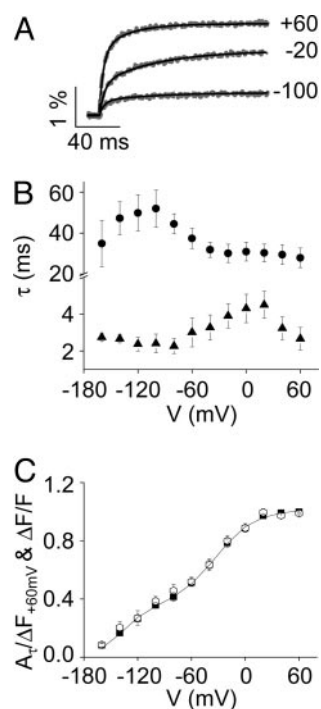

Fig. 3. Kinetic components of $\Delta F/F$. (A) $\Delta F/F$ traces (dashed gray lines) were obtained in the absence of Mg^{2+} by stepping from -180 mV to the indicated voltages, and fitted with two exponential components (solid black lines). Representative data are shown. (B) Fitted values of τ_{slow} (circles) and τ_{fast} (triangles), presented as mean $\pm$ SEM ($n = 4$–8), have been plotted versus test potential. (C) Values of $A_\tau/\Delta F_{+60\ mV}$ (open symbols), presented as mean $\pm$ SEM ($n = 8$), have been plotted versus test potential. For comparison, the $\Delta F/F$–V data points (filled symbols) and fitted curve (solid line) from Fig. 1D are also shown.

(Fig. 4B). In contrast, Mg^{2+} did not appear to shift the voltage dependence of τ_{fast} (Fig. 4B).

The Mg^{2+}-induced shift in the voltage dependence of τ_{slow} was also apparent when the contribution of τ_{slow} to the overall kinetics of the $\Delta F/F$ signal was plotted as a function of voltage. Fig. 4C shows the relative fitted amplitudes of the slow (A_{slow}) and fast (A_{fast}) kinetic components of the $\Delta F/F$ signal in the absence and presence of Mg^{2+}. In the absence of Mg^{2+}, τ_{fast} became the major determinant of $\Delta F/F$ kinetics at 0 mV (Fig. 4C Upper). In contrast, in the presence of Mg^{2+}, τ_{fast} did not predominate until $+40$ mV (Fig. 4C Lower). These results indicate that the voltage dependence of A_{slow} was shifted ≈ 40 mV in the depolarized direction in the presence of Mg^{2+}, similar to the shift in the values of τ_{slow}.

Steady-State Components of $\Delta F/F$ Are Differentially Modulated by Mg^{2+}. As shown in Fig. 5A, Mg^{2+} shifted the voltage dependence of the $\Delta F/F$ kinetics ($A_\tau/\Delta F_{+60\ mV}$–$V$ curve) in the depolarized direction. The effect was more prominent in the hyperpolarized voltage range, consistent with the larger effect of Mg^{2+} on the slow kinetic component. Mg^{2+} similarly shifted the steady-state $\Delta F/F$–V curve (Fig. 5B), confirming the correspondence between the kinetic and steady-state components of the $\Delta F/F$ signal. To characterize the effect of Mg^{2+} on the steady-state components of the $\Delta F/F$ signal, the $\Delta F/F$–V data were fitted with two Boltzmann components. The hyperpolarized component was shifted by approximately $+20$ mV, whereas the depolarized component was shifted less, by approximately $+10$ mV (Fig. 5C). These results confirm that Mg^{2+} preferentially affects activation transitions that occur at hyperpolarized voltages. For comparison, we reported previously that Mg^{2+} does not shift the
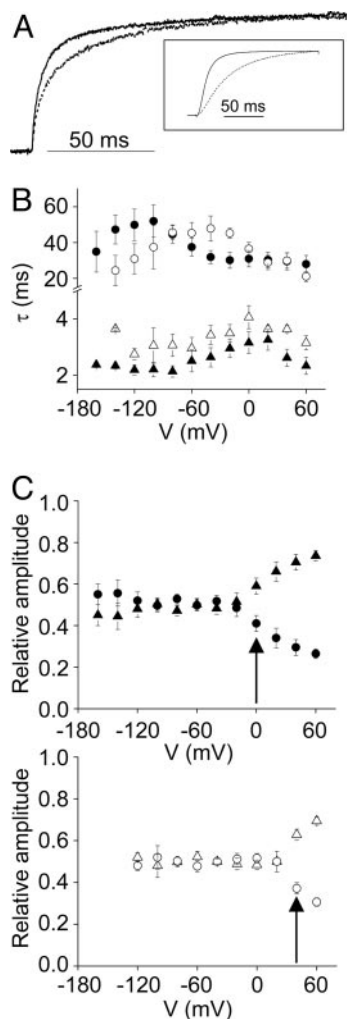
PHYSIOLOGY

Fig. 4. Mg^{2+} modulates $\Delta F/F$ kinetics. (*A*) (*Inset*) Representative TMRM-L342C ionic currents were recorded in the absence (solid) or presence (dashed) of 10 mM Mg^{2+} by stepping from -180 to 0 mV. Traces were scaled to the same amplitude. The main panel shows representative scaled $\Delta F/F$ traces, recorded in the absence (solid) or presence (dashed) of 10 mM Mg^{2+} by stepping from -180 to 0 mV. (*B*) Fitted values of τ_{slow} (circles) and τ_{fast} (triangles), obtained in the absence (filled symbols) or presence (open symbols) of 10 mM Mg^{2+}, have been plotted versus test potential. Data are presented as mean $\pm$ SEM ($n = 4$–8). (*C*) Fitted relative amplitudes of the slow (A_{slow}, circles) and fast (A_{fast}, triangles) kinetic components of $\Delta F/F$ were obtained in the absence (*Upper*) or presence (*Lower*) of Mg^{2+} and plotted versus test potential. The arrows indicate the voltages where the fast component becomes predominant. Data are presented as mean $\pm$ SEM ($n = 4$–8).

G–V or *Q–V* curves by >5 or 10 mV, which was not statistically significant (16).

$\Delta F/F$ Signal Can Account for eag Activation Kinetics in the Presence and Absence of Mg^{2+}. Our data indicate that the $\Delta F/F$ signal reports ion-modulated rate-determining conformational changes of the eag voltage sensor, including transitions that cannot be detected electrically. If so, the kinetics of the $\Delta F/F$ signal should account for the time course of eag activation in the absence and presence of extracellular Mg^{2+}. To test this, we overlaid the ionic currents with $\Delta F/F$ traces (Fig. 6). As noted above, the time course of the $\Delta F/F$ signal precedes ionic current activation (see Fig. 1*B*). However, in tetrameric K^+ channels, voltage sensor conformational changes that initiate activation occur independently in each of the subunits before a final
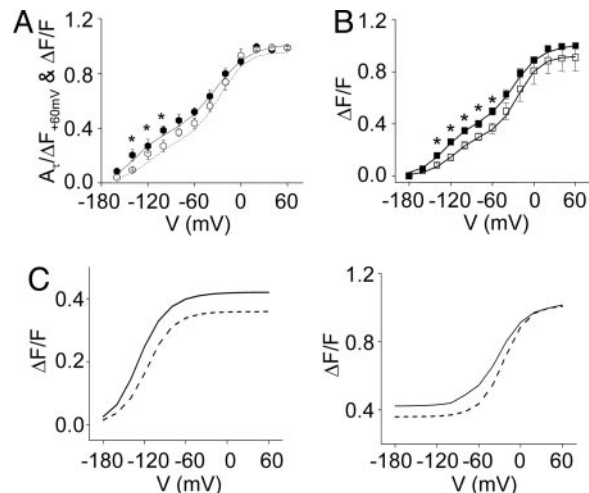

Fig. 5. Comparison of the effect of Mg^{2+} on the kinetic and steady-state components of $\Delta F/F$. (*A*) $A_\tau/\Delta F_{+60\,mV} - V$ curves were obtained in the absence (filled circles) or presence (open circles) of Mg^{2+}. Data are shown as mean $\pm$ SEM, $n = 4$–9 ($*, P < 0.05$, one-way ANOVA). For comparison, double Boltzman fits to the $\Delta F/F$–V data obtained in the absence (solid line) or presence (dashed line) of Mg^{2+} are also shown (see *B*). (*B*) Normalized steady-state $\Delta F/F$–V curves were obtained in the absence (filled squares) or presence (open squares) of Mg^{2+}. Each curve was fitted by the sum of two Boltzmann functions (solid lines). In the presence of Mg^{2+}, $V_{1/2}$ values for the hyperpolarized and depolarized components were -108 ± 1.7 mV and -20 ± 0.1 mV, respectively. Both components had apparent valences of 0.7 ± 0.1. For fitted values of $V_{1/2}$ and z in the absence of Mg^{2+}, see Fig. 1 legend. Data are shown as mean $\pm$ SEM, $n = 4$–9 ($*, P < 0.05$, one-way ANOVA). (*C*) The fitted hyperpolarized (*Left*) and depolarized (*Right*) steady-state components of $\Delta F/F$ in the absence (solid line) and presence (dashed line) of Mg^{2+} are shown.

cooperative transition that opens the pore (15, 33–35). All four voltage sensors must be in a permissive conformation for the pore to open. This requirement was approximated by raising $\Delta F/F$ to the fourth power. The plot of $(\Delta F/F)^4$ showed excellent agreement with the complex sigmoidal kinetics of the initial activation of the ionic conductance in the absence and in the presence of Mg^{2+} (Fig. 6; see also Fig. 9, which is published as supporting information on the PNAS web site). We conclude that the conformational changes underlying the $\Delta F/F$ signal determine the kinetics of eag activation and account for its modulation by extracellular Mg^{2+}.

Discussion

Mg^{2+} slows eag ionic currents much more than gating currents, suggesting that Mg^{2+} modulates voltage sensor conformational
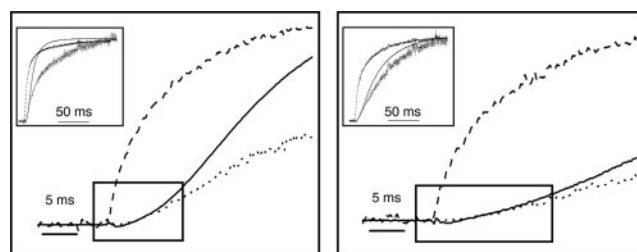

Fig. 6. $(\Delta F/F)^4$ accounts for eag activation kinetics. (*Insets*) Representative normalized $\Delta F/F$ (dashed), ionic current (solid), and $(\Delta F/F)^4$ (dotted) traces were obtained in the absence (*Left*) or presence (*Right*) of 10 mM Mg^{2+} by pulsing from -180 to 0 mV. The maximum amplitudes of $\Delta F/F$ and I, obtained at the end of the records, were scaled to a value of 1.0 before calculating $(\Delta F/F)^4$. Shown are the same data as the *Insets*, but using an expanded time scale. The boxes highlight the complex sigmoidal kinetics of the initial activation of the ionic conductance.

changes that are poorly represented in gating current recordings (16). To test this hypothesis, we chose an optical approach, because voltage-dependent changes in fluorescent intensity from a suitably located probe would not depend on the amount or kinetics of gating charge movement, making it feasible to detect transitions that transfer relatively little charge or occur slowly. Using a fluorescent probe attached to the N-terminal end of the S4 segment, we detected two phases of the activation process in eag channels. One phase corresponds to the main charge-moving conformational changes of the voltage sensor. These transitions generate the detectable gating currents. The other phase occurs in a more hyperpolarized voltage range where we have not detected gating currents. Nevertheless, we have obtained strong evidence that this component of the $\Delta F/F$ signal reflects part of the activation pathway in eag, and in particular corresponds to the rate-determining conformational changes of the voltage sensor that are accessed by prepulse hyperpolarization. These slow transitions are prominently modulated by extracellular Mg^{2+}. In the presence of Mg^{2+}, the slow kinetic component of $\Delta F/F$, which has a hyperpolarized voltage dependence, is shifted ≈ 60 mV in the depolarized direction. This result is consistent with our previous finding that Mg^{2+} shifts the range of prepulse potentials that elicit the steepest change in activation kinetics to more depolarized potentials (see figure 3C in ref. 16). The strongest evidence that both phases of the $\Delta F/F$ signal correspond to voltage sensor transitions is that $(\Delta F/F)^4$ accounts for the complex sigmoidal kinetics of the ionic currents in both the presence and absence of Mg^{2+}. The fourth-power dependence indicates that the gating transitions reported by $\Delta F/F$ occur independently in each of the four subunits of the channel.

Despite the fact that no gating currents were detected in the voltage range of the hyperpolarized component of $\Delta F/F$, the $\Delta F/F$ signal is clearly voltage-dependent. Thus, the underlying voltage sensor transitions must have some gating-charge movement associated with them. Our results indicate that this charge movement is too small or too slow to be detected electrically. The optical method is ideally suited to detect these transitions, because it is not subject to these limitations.

Conclusion

We have used a fluorescent reporter to detect voltage sensor conformational changes that have not been detected electrically. The fluorescent signal accounts for the time course of eag activation and its modulation by extracellular divalent cations. Transitions detected by the optical probe therefore account for the quantitatively different effects of Mg^{2+} on ionic and gating currents.

1. Warmke, J., Drysdale, R. & Ganetzky, B. (1991) *Science* **252,** 1560–1562.
2. Warmke, J. W. & Ganetzky, B. (1994) *Proc. Natl. Acad. Sci. USA* **91,** 3438–3442.
3. Sanguinetti, M. C., Jiang, C., Curran, M. E. & Keating, M. T. (1995) *Cell* **81,** 299–307.
4. Saganich, M. J., Machado, E. & Rudy, B. (2001) *J. Neurosci.* **21,** 4609–4624.
5. Curran, M. E., Splawski, I., Timothy, K. W., Vincent, G. M., Green, E. D. & Keating, M. T. (1995) *Cell* **80,** 795–803.
6. Sanguinetti, M. C. & Mitcheson, J. S. (2005) *Trends Pharmacol. Sci.* **26,** 119–124.
7. MacKinnon, R. (1991) *Nature* **350,** 232–235.
8. Doyle, D. A., Morais Cabral, J., Pfuetzner, R. A., Kuo, A., Gulbis, J. M., Cohen, S. L., Chait, B. T. & MacKinnon, R. (1998) *Science* **280,** 69–77.
9. Jiang, Y., Lee, A., Chen, J., Ruta, V., Cadene, M., Chait, B. T. & MacKinnon, R. (2003) *Nature* **423,** 33–41.
10. Tempel, B. L., Papazian, D. M., Schwarz, T. L., Jan, Y. N. & Jan, L. Y. (1987) *Science* **237,** 770–775.
11. Aggarwal, S. K. & MacKinnon, R. (1996) *Neuron* **16,** 1169–1177.
12. Seoh, S. A., Sigg, D., Papazian, D. M. & Bezanilla, F. (1996) *Neuron* **16,** 1159–1167.
13. Bezanilla, F. (2000) *Physiol. Rev.* **80,** 555–592.
14. Terlau, H., Ludwig, J., Steffan, R., Pongs, O., Stühmer, W. & Heinemann, S. H. (1996) *Pflügers Arch.* **432,** 301–312.
15. Schönherr, R., Hehl, S., Terlau, H., Baumann, A. & Heinemann, S. H. (1999) *J. Biol. Chem.* **274,** 5362–5369.
16. Tang, C.-Y., Bezanilla, F. & Papazian, D. M. (2000) *J. Gen. Physiol.* **115,** 319–337.
17. Silverman, W. R., Tang, C.-Y., Mock, A. F, Huh, K.-B. & Papazian, D. M. (2000) *J. Gen. Physiol.* **116,** 663–677.
18. Silverman, W. R., Bannister, J. P. A. & Papazian, D. M. (2004) *Biophys. J.* **87,** 3110–3121.
19. Silverman, W. R., Roux, B. & Papazian, D. M. (2003) *Proc. Natl. Acad. Sci. USA* **100,** 2935–2940.
20. Timpe, L. C., Schwarz, T. L., Tempel, B. L., Papazian, D. M., Jan, Y. N. & Jan, L. Y. (1988) *Nature* **331,** 143–145.
21. Papazian, D. M., Timpe., L. C., Jan, Y. N. & Jan, L. Y. (1991) *Nature* **349,** 305–310.
22. Stefani, E., Toro, L., Perozo, E. & Bezanilla, F. (1994) *Biophys. J.* **66,** 996–1010.
23. Cha, A. & Bezanilla, F. (1998) *J. Gen. Physiol.* **112,** 391–408.
24. Bezanilla, F. & Armstrong, C. M. (1977) *J. Gen. Physiol.* **70,** 549–566.
25. Cha, A. & Bezanilla, F. (1997) *Neuron* **19,** 1127–1140.
26. Chanda, B., Asamoah, O. K. & Bezanilla, F. (2004) *J. Gen. Physiol.* **123,** 217–230.
27. Mannuzzu, L. M., Moronne, M. M. & Isacoff, E. Y. (1996) *Science* **271,** 213–216.
28. Schönherr, R., Mannuzzu, L. M., Isacoff, E. Y. & Heinemann, S. H. (2002) *Neuron* **35,** 935–949.
29. Smith, P. L. & Yellen, G. (2002) *J. Gen. Physiol.* **119,** 275–293.
30. Kozak, M. (1987) *J. Mol. Biol.* **196,** 947–950.
31. Cole, K. S. & Moore, J. W. (1960) *Biophys. J.* **1,** 1–14.
32. Taylor, R. E. & Bezanilla, F. (1983) *J. Gen. Physiol.* **81,** 773–784.
33. Bezanilla, F., Perozo, E. & Stefani, E. (1994) *Biophys. J.* **66,** 1011–1021.
34. Zagotta, W. N., Hoshi, T. & Aldrich, R. W. (1994) *J. Gen. Physiol.* **103,** 321–362.
35. Schoppa, N. E. & Sigworth, F. J. (1998) *J. Gen. Physiol.* **111,** 313–342.

PHYSIOLOGY